INSTITUTE OF PHYSICS PUBLISHING SUPERCONDUCTOR SCIENCE AND TECHNOLOGY
Supercond. Sci. Technol. **16** (2003) 71–79 PII: S0953-2048(03)40107-3

An improved method for quantitative magneto-optical analysis of superconductors

F Laviano[1,2,3], D Botta[1,2,3], A Chiodoni[1,2,3], R Gerbaldo[1,2,3], G Ghigo[1,2,3], L Gozzelino[1,2,3], S Zannella[4] and E Mezzetti[1,2,3]

[1] Istituto Nazionale per la Fisica della Materia, U.d.R. Torino-Politecnico, c.so Duca Degli Abruzzi 24, 10129 Torino, Italy
[2] Istituto Nazionale di Fisica Nucleare, Sez. Torino, via P. Giuria 1, 10125 Torino, Italy
[3] Department of Physics, Politecnico di Torino, c.so Duca degli Abruzzi 24, 10129 Torino, Italy
[4] EDISON TERMOELETTRICA S.p.a., Foro Bonaparte 31, Milano, Italy

Received 31 July 2002, in final form 15 October 2002
Published 10 December 2002
Online at stacks.iop.org/SUST/16/71

Abstract
We report on the analysis method to extract quantitative local electrodynamics in superconductors by means of the magneto-optical technique. First of all, we discuss the calibration procedure to convert the local light intensity values into magnetic induction field distribution and start focusing on the role played by the generally disregarded magnetic induction components parallel to the indicator film plane (in-plane field effect). To account for the reliability of the whole technique, the method used to reconstruct the electrical current density distribution is reported, together with a numerical test example. The methodology is applied to measure local magnetic field and current distributions on a typical $YBa_2Cu_3O_{7-x}$ good quality film. We show how the in-plane field influences the MO measurements, after which we present an algorithm to account for the in-plane field components. The meaningful impact of the correction on the experimental results is shown. Afterwards, we discuss some aspects about the electrodynamics of the superconducting sample.

(Some figures in this article are in colour only in the electronic version)

1. Introduction

The magneto-optical (MO) technique is a powerful tool to examine the local magnetic field distribution over the surface of a superconducting sample [1–3]. The main advantage of the MO tool with respect to other magnetic field imaging techniques, such as SQUID or μHall-probe array scanning magnetometry, is the parallel measurement on each point of the interested surface, which allows the precise and local evaluation of electrodynamical quantities (B, J, E) [3] and the observation of local dynamic phenomenology [4].

The conventional MO measurement process results in a set of images representing the surface of a ferromagnetic indicator film that is placed over the flat superconductor. Throughout the Faraday effect, the indicator film with in-plane anisotropy [5], hit by linearly polarized light, shows the changes in its local magnetic moment due to external magnetic field as local light intensity modulation. The quantitative analysis starts with the calibration process where the local light intensity of the images is converted into local magnetic induction values. Generally, only the perpendicular component of the magnetic induction is considered in the calibration process, whereas the in-plane components are disregarded. Although in the case of thin samples, the measurement of the magnetic induction component perpendicular to the superconductor surface alone does suffice to rebuild the electrical current density distribution, in a 'model-independent' way by the numerical inversion of the Biot–Savart law [3], the supercurrents always induce in-plane magnetic field components at the superconductor surfaces and, as shown in [6, 7], the indicator

film strongly reacts to the in-plane components too. Then, the inversion process results in misleading features in the current density distribution if the in-plane field effect is not accounted for. In this work, we show how to extend the one-dimensional in-plane field effect correction [6] to a 'model-independent' two-dimensional and iterative algorithm which evaluates the full magnetic induction distribution on the superconductor surface and the in-plane current density distribution with high accuracy.

The paper is organized as follows. The experimental apparatus is briefly described in section 2. In section 3, we report on the calibration procedure of the MO image data. Here, we start focusing on the electrodynamical model of the indicator film that accounts for the effect of the in-plane magnetic fields. The inversion procedure of the Biot–Savart law, which follows a method developed by Roth [8] and applied to MO analysis by Jooss [3, 9], is described in detail and verified in section 4. In section 5, the method is applied to the experimental results obtained with conventional MO analysis, which are affected by the in-plane field effect. The iterative procedure, designed to correct the MO measurements from the in-plane field effect, is described in section 6. Then, we make a first comparison between the precise quantitative information obtained by the MO investigation of the superconductor and known models concerning the distribution of the electrodynamic fields (B, J) inside the sample. The results and comments are presented in section 7. Finally, we resume our conclusions in section 8.

2. Experimental set-up

Our experimental set-up for magneto-optical analysis is depicted in figure 1. The microscope is a Optiphot© by Nikon™, equipped with a Glan-Thompson polarizer and a rotating polarization analyser. Outside the mirror, there is an exciting filter in the wavelength range centred at 530 nm, in order to obtain the maximum Faraday rotation from the indicator film. The magnetic sensors are Bi-doped ferrite garnets with in-plane anisotropy (thickness 2–5 μm), grown on a GGG transparent substrate; on the other face, an Al mirror and a protective layer are deposited (both of them have thickness of about 150 nm). For details on the physical properties of these indicator films, see [10].

The cryostat is a custom-design by Oxford™ with continuous flow of refrigerator liquid; a heater and a temperature controller allow working temperatures ranging from 3.5 K to 350 K. The video camera is a monochromatic 12 bit digital camera (Adimec™ MX12P©) with a CCD matrix of 1024 × 1024 pixels. Other details of our apparatus can be found in [11].

3. Conversion of the MO images into magnetic induction values

The light intensity of the pixels in MO images carries information about the local magnetic field at the indicator plane. To extract this information, we consider a suitable electrodynamical model to account for the indicator film behaviour [6]. With reference to figure 2, the interaction

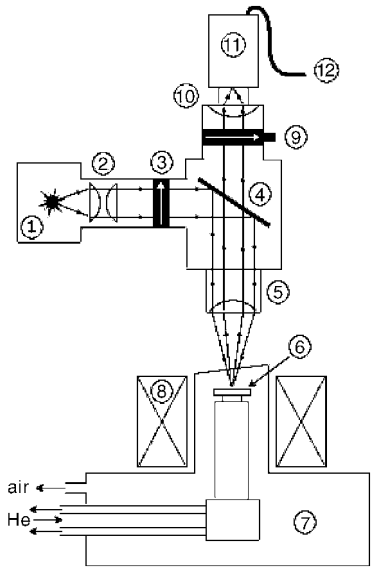

Figure 1. Scheme of our experimental set-up. The light beam, from the Hg lamp (1), is collimated by a biconvex lens (2) before passing through a polarizer (3). After the exciting filter (not drawn), the light hits a beam splitter (4) and is focused by the objective lens (5) onto the indicator surface (6). The indicator film is put over the superconducting sample inside the cryostat (7). An external magnet (8), cooled with water, generates a uniform magnetic field in the direction perpendicular to the indicator plane. The refracted light passes through the lens (5), the beam-splitter (4) and the rotating analyser (9), before being focalized by the camera lens (10) and captured in the CCD matrix of the video camera (11). A personal computer (12-not drawn) picks up the digital signal of the camera and elaborates it.

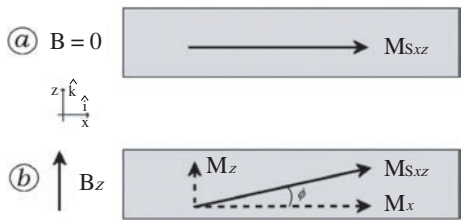

Figure 2. Abstract view of the indicator film cross section (only the M_S projections to xz plane are depicted). (a) When there is no external magnetic excitation, the spontaneous magnetization vector lies in the film plane. (b) An external magnetic field perturbs the local magnetization of the indicator. The field component perpendicular to the film surface is responsible for the rotation of the spontaneous magnetization out of the indicator plane.

energy E_{int} of the system (indicator film) with magnetic field B can be evaluated as

$$E_{\text{int}} = E_{\text{A}}(1 - \cos\phi) + BM_{\text{S}}[1 - \cos(\alpha - \phi)] \qquad (3.1)$$

where E_{A} is the anisotropy energy, M_{S} is the value of spontaneous magnetization and α is the angle formed between the magnetic induction vector and the xy plane, where the spontaneous magnetization lies with no external fields. The angle ϕ accounts for the perturbation of the magnetic moments inside the ferrite; the derivative of (3.1), with respect to ϕ, yields the equilibrium position

$$\phi = \arctan\frac{B_z}{B_{xy} + B_{\text{A}}} \qquad (3.2)$$

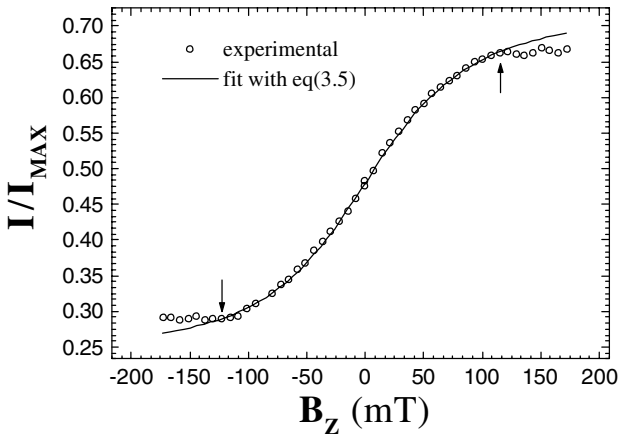

Figure 3. Example of a calibration curve. The points are the light intensity (normalized after the division by the maximum intensity image) in a pixel on the indicator surface ($T = 5$ K, $\theta = 45° = 0.7854$ rad). The line is the fit with equation (3.5). The fitting procedure yields the values of the three parameters needed for the conversion of the light intensity values into magnetic induction ones ($\chi^2 = 8.145 \times 10^{-6}$, $CM_S = 0.2508 \pm 0.0038$, $B_A = 99.9 \pm 2.5$, $I_0 = -0.020\,90 \pm 0.000\,48$). The two arrows indicate the saturation field of the indicator, above which no information on the local field can be resolved. Then we limit our analysis on the images containing points with maximum local field below the saturation threshold.

with $B_A = E_A/M_S$, $B_z = \mathbf{B} \cdot \hat{\mathbf{k}} = B \sin\alpha$ and $B_{xy} = \sqrt{(\mathbf{B} \cdot \hat{\mathbf{i}})^2 + (\mathbf{B} \cdot \hat{\mathbf{j}})^2} = B \cos\alpha$.

The polarization plane of the incident light is rotated by the Faraday effect, and the amount of rotation, indicated by the angle α_F, is proportional to the magnetization component along the light direction. We disregard the dispersion of light path lengths because, in the considered configuration, deviations to perpendicular light on the indicator surface are much less than other polarization 'losses'. Then we assume the simple relation (see figure 2)

$$\alpha_F = C M_S \sin\phi \tag{3.3}$$

where C is a parameter which depends on the thickness of the indicator film. All the parameters characterizing the ferrite garnet strongly depend on the temperature as well as on the wavelength of the light. Here it is supposed that the measurements are isothermal and performed with monochromatic light, so for each temperature we make a distinct calibration process and all parameters are taken as constants.

The Faraday rotation is detected by the analyser, which is fixed at an angle θ off the polarizer direction. From the Malus law, the light intensity I received by the video camera is

$$I = I_0 + I_{MAX} \cos^2(\alpha_F + \theta). \tag{3.4}$$

I_{MAX} is the light intensity of the incident beam and I_0 is the intensity of the non-linear polarized light (this parameter and θ also model the polarization losses across the optical path). Combining equation (3.4) with (3.3) and (3.2), we obtain the relation between the measured light intensity and the magnetic induction:

$$I = I_0 + I_{MAX} \cos^2\left[\frac{C M_S B_z}{\sqrt{(B_A + B_{xy})^2 + B_z^2}} + \theta\right]. \tag{3.5}$$

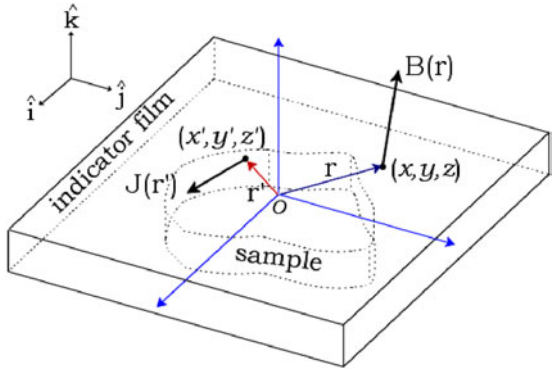

Figure 4. Reference system. The origin of the axis is put onto a plane at half the thickness of the sample. The distance between the top surface of the sample and the indicator film is h.

This equation demonstrates that the indicator film reacts also with the in-plane components of the magnetic induction. As we will see in more detail later, this contribution increases with higher electrical currents and with increasing thickness of the sample. In any case, the effect of the in-plane field consists in the apparent increasing of the local anisotropy field.

Equation (3.5) can be used for the calibration procedure, after we have collected the light intensity measurements of a point over the indicator film surface under the action of a known value of the magnetic induction field. This can be achieved in a zone far enough from the area influenced by the field generated by the sample, where the Faraday rotation is only determined by the externally applied field which is uniform and perpendicular to the indicator plane. In this case, there is no action of in-plane fields.

The required $I(B_z)$ data are collected by means of an isothermal magnetization cycle: the external magnetic field is increased discontinuously in steps and for each step we acquire a MO image. The procedure can vary in different experiments: zero field cooling or field cooling of the sample, relaxation measurements, etc. In any case, the complete ramp of applied dc fields is needed for the calibration.

Figure 3 shows a typical calibration curve. The points are the light intensity values of a single pixel, belonging to a zone far from the sample, and the solid line is the calibration curve obtained by fitting the experimental data with equation (3.5). We can determine experimentally two parameters: the angle θ and I_{MAX}, as the image acquired with the polarizer parallel to the analyser. In the case of the measurements presented here, this procedure yields a magnetic resolution of about 1 mT (for magnetic fields ranging from 1 mT to about 130 mT). The calibration procedure described here allows obtaining the local value (with sign) of the magnetic induction component in the z direction, for arbitrary external fields and instants of time, but always at a fixed temperature. The time resolution is only limited by the acquisition hardware (e.g. for our frame grabber the time step is 40 ms).

4. The inversion method

The magnetic induction field in a point over the indicator surface is the superposition of the field generated by the

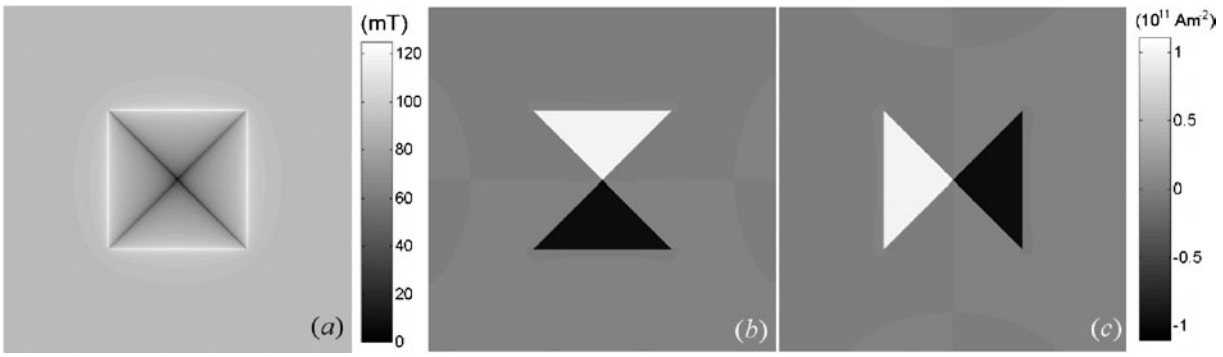

Figure 5. Calculated magnetic field map and current density distributions. (*a*) Magnetic induction field (z component) distribution on the top surface of a square superconducting sample in fully developed Bean critical state. The following parameters were used for this map (1500 × 1500 pixels): external applied field (perpendicular to the image, positive from the paper to the reader) of 90 mT, critical current density of 10^{11} A m^{-2}, sample thickness of 300 nm. (*b*) and (*c*) Electrical current density distribution for J_x and J_y components, respectively, calculated by applying the inversion method to the field map reported in (*a*). The figures show the local values with sign of the two electrical current density components; positive values mean the current density vector is directed from bottom to top (y) or from left to right (x). The small modulations on the borders of the image and of the current density distribution are due to the finite frequency spectrum utilized and represent the error of the inversion procedure. Their values are four to five orders of magnitude less than the signal.

superconductor, $H_{\rm ind}$, and the sum of all the magnetic sources external to it, $H_{\rm ext}$. In SI units

$$\mathbf{B}(\mathbf{r}) = \mu_0(\mathbf{H}_{\rm ext}(\mathbf{r}) + \mathbf{H}_{\rm ind}(\mathbf{r})). \tag{4.1}$$

The electrical current density, flowing inside the sample ($\nabla \cdot \mathbf{J}(\mathbf{r}) = 0$), induces a magnetic field according to the Biot–Savart law:

$$\mu_0\mathbf{H}_{\rm ind}(\mathbf{r}) = \frac{\mu_0}{4\pi}\int \frac{\mathbf{J}(\mathbf{r}')\wedge(\mathbf{r}-\mathbf{r}')}{|\mathbf{r}-\mathbf{r}'|}\,\mathrm{d}^3r'. \tag{4.2}$$

Each component of the induced field is generated by two components of the electrical current density field (with reference to figure 4):

$$\mu_0\mathbf{H}_{\rm ind}\cdot\hat{\mathbf{i}} = \mu_0 H_x(x,y,z) = \frac{\mu_0}{4\pi}\iiint \frac{J_y(x',y',z')(z-z') - J_z(x',y',z')(y-y')}{\sqrt{[(x-x')^2+(y-y')^2+(z-z')^2]^3}} \times \mathrm{d}x'\,\mathrm{d}y'\,\mathrm{d}z' \tag{4.3}$$

$$\mu_0\mathbf{H}_{\rm ind}\cdot\hat{\mathbf{j}} = \mu_0 H_y(x,y,z) = \frac{\mu_0}{4\pi}\iiint \frac{J_z(x',y',z')(x-x') - J_x(x',y',z')(z-z')}{\sqrt{[(x-x')^2+(y-y')^2+(z-z')^2]^3}} \times \mathrm{d}x'\,\mathrm{d}y'\,\mathrm{d}z' \tag{4.4}$$

$$\mu_0\mathbf{H}_{\rm ind}\cdot\hat{\mathbf{k}} = \mu_0 H_z(x,y,z) = \frac{\mu_0}{4\pi}\iiint \frac{J_x(x',y',z')(y-y') - J_y(x',y',z')(x-x')}{\sqrt{[(x-x')^2+(y-y')^2+(z-z')^2]^3}} \times \mathrm{d}x'\,\mathrm{d}y'\,\mathrm{d}z'. \tag{4.5}$$

In principle, the information from a non-invasive measurement is not enough to solve the full 3D inverse problem [8]. The unique and exact solution can be found for the 2D inverse problem, where the electrical current density distribution is considered constant over the z direction. This is true for samples flat and thin, i.e. with $d < 2\lambda$ [12]. Otherwise, the measured quantities must be considered as averaged over the thickness. Therefore, regarding the 2D problem, the equation to be inverted is

$$\mu_0 H_z(x,y,h) = \frac{\mu_0}{4\pi}\int_{-d/2}^{d/2}\iint \frac{J_x(x',y')(y-y') - J_y(x',y')(x-x')}{\sqrt{[(x-x')^2+(y-y')^2+(h-z')^2]^3}} \times \mathrm{d}x'\,\mathrm{d}y'\,\mathrm{d}z'. \tag{4.6}$$

The inversion problem can be dealt with different approaches (a direct one is the matrix inversion, see [13, 14]). We follow the arguments of Roth *et al* [8]: the Biot–Savart law has translational symmetry, thus we can apply the convolution theorem. This method was developed and applied to MO technique by Jooss [3, 9], who treated more accurately the finite thickness of the sample. By two-dimensional Fourier transformation, equation (4.6) transforms into

$$\mu_0\tilde{H}_z(k_x,k_y,h) = \mathrm{i}\frac{\mu_0}{2}\int_{-d/2}^{d/2}\left(\frac{k_y}{\sqrt{k_x^2+k_y^2}}\tilde{J}_x(k_x,k_y) - \frac{k_x}{\sqrt{k_x^2+k_y^2}}\tilde{J}_y(k_x,k_y)\right)\mathrm{e}^{-(h-z')\sqrt{k_x^2+k_y^2}}\,\mathrm{d}z'. \tag{4.7}$$

The integration over the thickness (variable z') can be done analytically and yields

$$\mu_0\tilde{H}_z(k_x,k_y,h) = \mathrm{i}\frac{\mu_0}{2}\left(\frac{k_y}{k}\tilde{J}_x(k_x,k_y) - \frac{k_x}{k}\tilde{J}_y(k_x,k_y)\right) \times \frac{\mathrm{e}^{-hk}}{k}\sinh\left(\frac{d}{2}k\right). \tag{4.8}$$

Using the condition for the electrical current density field to flow only inside the sample (i.e. $\nabla\cdot\mathbf{J}(\mathbf{r}) = 0$ with the assumption that $\partial J_z/\partial_z = 0$), we obtain a solvable system:

$$\begin{cases}\mu_0\tilde{H}_z(k_x,k_y,h) = \mathrm{i}\frac{\mu_0}{2}\tilde{J}_x(k_x,k_y)\frac{\mathrm{e}^{-hk}}{k_y}\sinh\left(\frac{d}{2}k\right)\\ \tilde{J}_x(k_x,k_y) = -\tilde{J}_y(k_x,k_y)\frac{k_x}{k_y}\end{cases}. \tag{4.9}$$

The solution of the system (4.9) is the electrical current density distribution ($J_x(x,y)$ and $J_y(x,y)$) in a plane parallel to the indicator one, with information on local current

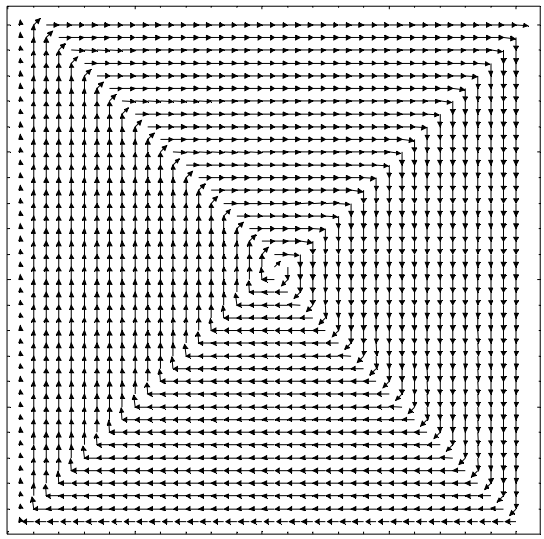

(*a*)

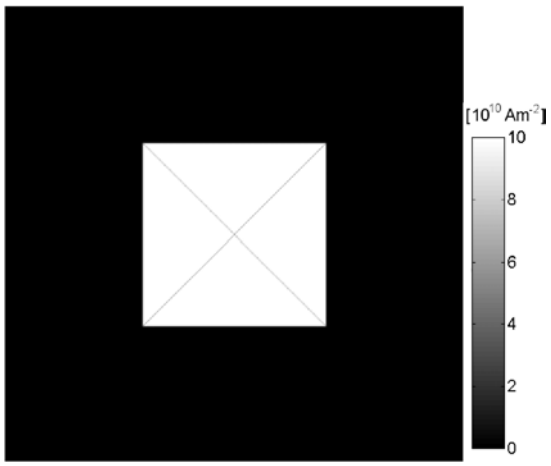

(*b*)

Figure 6. (*a*) Vector sum of the two current density components ($J_x(x, y)$ and $J_y(x, y)$). (*b*) Modulus distribution of the current density. As expected in the full-penetrated Bean critical state for this geometry, the electrical current density is uniform, flows parallel to the edges and bends near the discontinuity lines [21].

density direction and its local magnitude. The Fourier transformation is carried out by a FFT algorithm, which costs $N_x N_y(1 + 2\log(N_x N_y))$ operations ($N_x N_y$ is the dimension of the MO image in pixels). Since the dimensions of the images are finite, the FFT transformation introduces a superlattice of spurious current distributions. These current cells interact with the real current distribution if the area outside the sample contained in the MO image is not large enough. If the measurements are contaminated by some background noise (introduced by the electronic systems), the data can be filtered in *k*-space by means of an Hanning window. For more details see [3, 8, 9]. We test our algorithm with an artificial distribution of magnetic induction values, calculated on the basis of the Bean critical state model for rectangular thin superconductors [15]. In figure 5, the magnetic induction field map and the corresponding

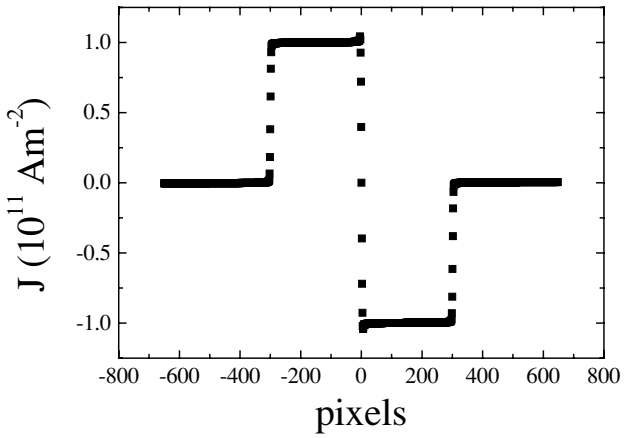

Figure 7. Profile along the central part of the current density map of figure 5(*c*). The current is constant in the sample, but changes direction crossing the centre. The plateau is located at 9.992×10^{10} A m^{-2}. The small peaks at the centre (less than ten pixels) are due to Gibbs oscillations because, in this theoretical model, the current density changes direction suddenly, i.e. with infinite frequency.

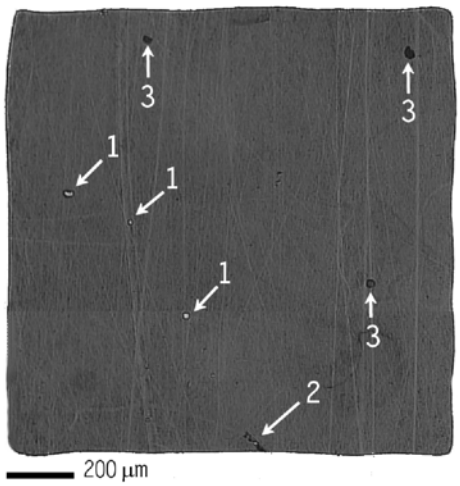

Figure 8. Optical image of the YBCO film. Four types of disorder are visible on the surface: some small holes produced during the etching process (1) (respectively, from top to bottom, the dimensions of the visible defects are 25×18, 7×7 and 15×15 μm^2); a deep scratch on the lower side (2); some impurities (3) and a soft pattern of lines, which do not disturb the electrical current flow into the superconducting film because they are located on the superficial non-superconducting layers.

current density distribution, obtained by the inversion method, are shown. The two electrical current density components, $J_x(x, y)$ and $J_y(x, y)$, can be combined to yield the direction pattern of the current or the local values of the current density modulus, as shown in figure 6. The result of the inversion is in excellent agreement with the theoretical distribution. In figure 7, the profile along the middle line of the square is presented. The value at the plateau differs less than 0.01% from the actual one.

5. Experimental results

We present the MO analysis on a $YBa_2Cu_3O_{7-\delta}$ (YBCO) film ($T_C = 88$ K, $\Delta T_C = 0.7$ K), grown by thermal co-evaporation

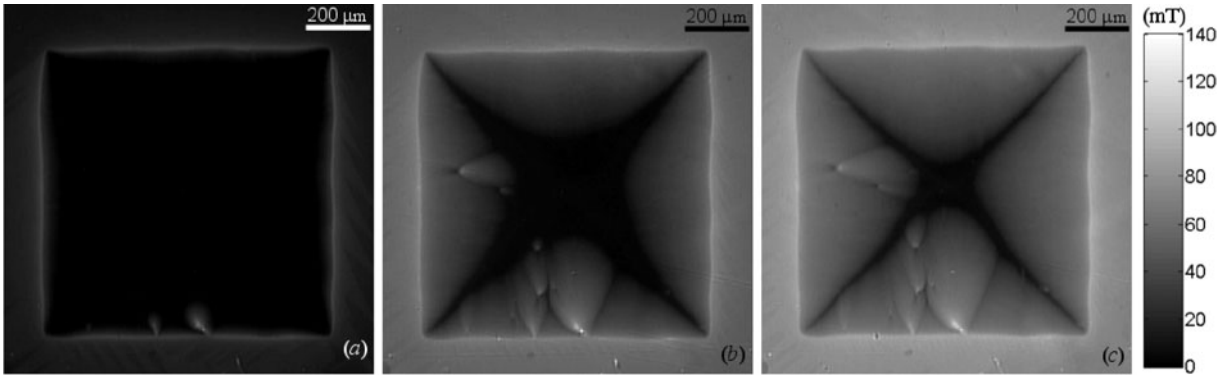

Figure 9. Magnetic induction distribution in the plane of the indicator film, along the direction perpendicular to the indicator plane (z). The maps were obtained from the corresponding magneto-optical images by means of the calibration procedure described in section 3. The area outside the sample necessary for a correct inversion procedure was partially cut for visual clarity. The measurement was carried at $T = 5$ K. (a) $\mu_0 H_{ext} = 14.6$ mT. The film is almost entirely in the Meissner state ($B = 0$), with the exclusion of the zone damaged by the cracks (bottom). (b) $\mu_0 H_{ext} = 46.2$ mT. At this stage, a part of the sample carries the vortices (nucleated from the edges) and sustains an electrical current to stop the flux motion due to Lorenz forces (i.e. a critical current). The cushion-like structure is characteristic of the rectangular geometry. The central part is flux free because of a Meissner current distribution. The holes and cracks have strongly perturbed the flux diffusion whereas in two quadrants (top and right) the flux profile is very homogeneous. (c) $\mu_0 H_{ext} = 69.2$ mT. Evolution of the flux diffusion near the fully penetrated critical state.

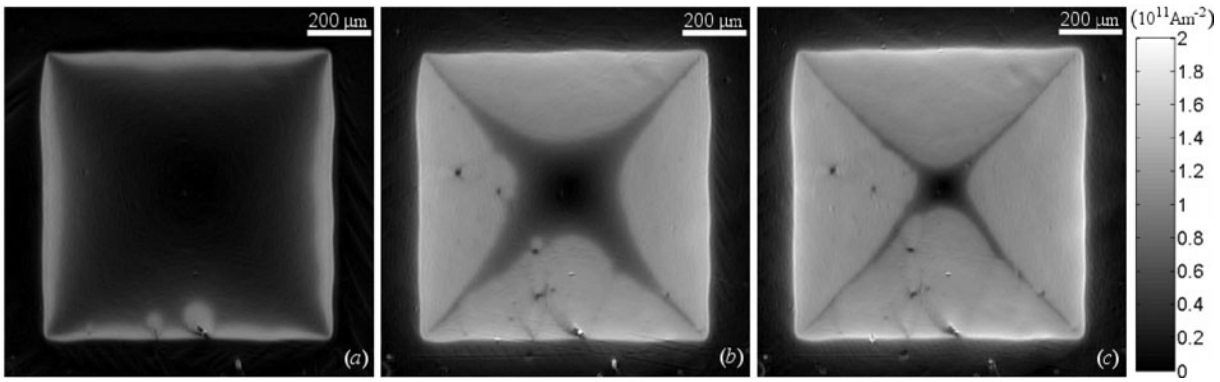

Figure 10. Electrical current density modulus distributions ($|J(x, y)| = \sqrt{J_X^2(x, y) + J_Y^2(x, y)}$) obtained by the inversions of the magnetic field maps reported in the previous figure. Everywhere the electrical current density is directed clockwise. (a) $\mu_0 H_{ext} = 14.6$ mT. The Meissner current flows in the whole sample volume. Its magnitude decreases continuously from the edges to the centre. (b) $\mu_0 H_{ext} = 46.2$ mT. The discontinuity lines (dark cross), where the electrical current bends, are more clearly visible in the penetrated zone. In the central part there is the remaining Meissner current distribution. (c) $\mu_0 H_{ext} = 69.2$ mT. The sample is near the full penetration and a strong current flows in almost the entire film. In this image, the unphysical high values of electrical current density outside the sample is more evident.

on an yttria stabilized zirconia (YSZ) substrate with a 40 nm thick CeO_2 buffer layer. The original deposition (square with 1 cm long sides, 400 nm thick) was chemically etched in order to obtain smaller squares with sides of about 1.25 mm. The optical image of the investigated sample is shown in figure 8. Three magnetic field maps, representative of a virgin magnetization cycle at $T = 5$ K, are presented in figure 9. These images show three different states during the magnetic flux diffusion inside the YBCO film: Meissner state, partly penetrated critical state and nearly full-penetrated critical state. The corresponding distributions of the electrical current density modulus, obtained by the inversion procedure, are presented in figure 10. Both magnetic field and electrical current density distributions qualitatively exhibit the well connected nanostructure of the YBCO film. With the exception of the visible microscopic defects (their influence is not discussed here), the flux front and the current pattern are arranged so as to obey the electrodynamical requirements imposed by the film geometry. In fact, the superconducting region is simply connected and there are no visible grain boundaries that penalize the electrical current flow pattern.

Besides the behaviour associated with the physical properties of the superconductor, we now focus on the unphysical result of non-zero current density distribution outside the sample. This effect can be noted clearly as a light shadow around the superconducting film, for example in figure 10(c). It can also be explored locally with line profiles, as those plotted in figure 11. The sample edges are located at the peaks of the current density curves and the spurious current density distribution appears as tails outside the superconductor. Moreover, the peaks of the current density at the edges and the curvature of the profiles are, by themselves, unexpected features. Since the inversion method works correctly, we argue

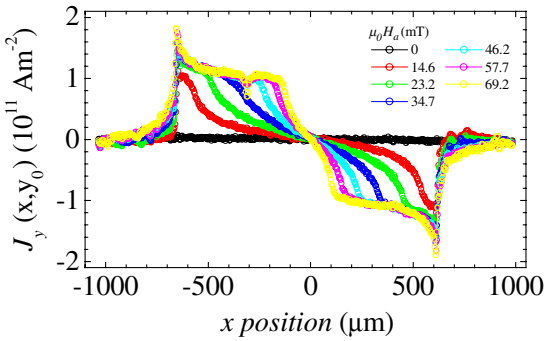

Figure 11. Linear profiles of the electrical current density modulus along the horizontal mid line of the squared film. The area occupied by the YBCO film is located between the peaks.

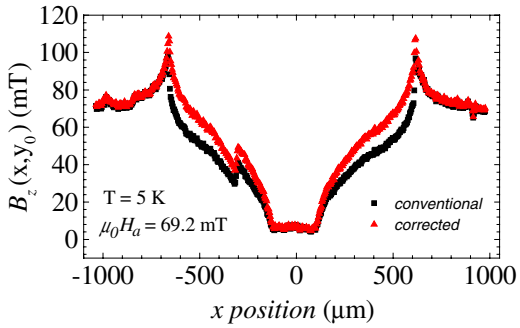

Figure 12. Comparison between two profiles of B_z, before and after the in-plane field correction, along the line displayed in figure 9(*c*).

that the cause resides in the measurement process, i.e. in the calibration procedure. In [6], this effect was observed by the MO technique (with a one-dimensional quantitative analysis) and was addressed to the magnetic field components directed in the plane of the indicator film. The only approximation we made working with the model (3.5) was just to ignore the in-plane magnetic field components, as commonly done in the standard MO calibration procedure [1–4, 14, 16]. In what follows, we relax the approximation of negligible in-plane magnetic fields and construct a 2D iterative procedure to correct the B_z maps.

6. In-plane field effect correction

The equation used to convert the light intensity values into magnetic induction field (z component) ones is the inverse of (3.5):

$$B_z = (B_A + B_{xy}) \tan \arcsin \left[\frac{1}{C M_S} \left(\arccos \sqrt{\frac{I - I_0}{I_{MAX}}} - \theta \right) \right]. \tag{6.1}$$

This equation can be rewritten as

$$B_z = \left(1 + \frac{B_{xy}}{B_A} \right) B_{z|o} \tag{6.2}$$

where $B_{z|o}$ is the equation obtained neglecting the B_{xy} contribution [6]. This relation holds locally: to correct the magnetic induction maps, we have to know the local values of $B_{xy} = \sqrt{(\mathbf{B} \cdot \hat{\mathbf{i}})^2 + (\mathbf{B} \cdot \hat{\mathbf{j}})^2}$. If the externally applied magnetic field is strictly directed along the z direction, the magnetic induction components parallel to the indicator plane are generated only by the electrical current flowing inside the superconductor. Equations (4.3) and (4.4) can be used to obtain these magnetic field components, but they require knowledge about the electrical current distribution along the z direction. We suppose that J_z is much lower than the in-plane components (as expected for the geometry of the investigated sample) and, as before, that the electrical current distribution is regarded as thickness averaged (z independent). We use the result of the inversion as the approximation of the real current density distribution to calculate the in-plane magnetic field components numerically by means of equations (4.3) and (4.4). The correction of the B_z maps follows, in a straightforward manner, from equation (6.2). This process can be iteratively repeated until the convergence is reached, following the scheme

$$B_z^{(n)}(x, y, h) \overset{\text{(Biot–Savart inversion)}}{\rightarrow} \left\{ J_x^{(n)}(x, y), J_y^{(n)}(x, y) \right\}$$
$$\overset{\text{equations (4.3) and (4.4)}}{\rightarrow} \left\{ B_x^{(n)}(x, y, h), B_y^{(n)}(x, y, h) \right\}$$
$$\overset{\text{equation (6.2)}}{\rightarrow} B_z^{(n+1)}(x, y, h).$$

The comparison between the magnetic induction values after and before the in-plane field correction is presented in figure 12. The difference of the B_z values inside the sample is remarkable: higher electrical current density results in larger contribution from the in-plane magnetic field. As shown in figure 13(*a*), the light shadow outside the sample has disappeared, i.e. now the current density vanishes outside the superconductor, in agreement with [6]. The profiles of current density modulus, during the correction process, are visible in figure 13(*b*). The complete series of profiles, i.e. at different external fields, are presented in figure 13(*c*).

7. Discussion

The remarkable difference between the first inversion result and the corrected one is due to the calibration procedure: the in-plane field generated by the supercurrents into the sample locally interacts with the indicator magnetic moments (see equation (3.2)), this effect is seen as a Faraday rotation reduction. So, if we convert the light intensity maps into B_z data, disregarding the in-plane field contribution, we underestimate locally the perpendicular magnetic induction component and, thus, the data contain a spurious magnetic field modulation. Because of the investigated sample geometry, the supercurrents induce *locally* an in-plane magnetic field, but their relation with the out-of-plane component is *non-local* [17]. Then, the spurious modulation corresponds to a fictitious current density distribution located inside the sample (where it is superimposed to the real one) and outside too.

The comparison between the series of profiles at different applied fields, figures 11 and 13(*c*), demonstrates that the correction depends only on the current density magnitude. After the correction, the edges of the sample overlap, careless of the applied magnetic field. Outside the sample, the residual signal is due to defects belonging to the indicator film (surface or bulk cracks, in-plane magnetic domain structures).

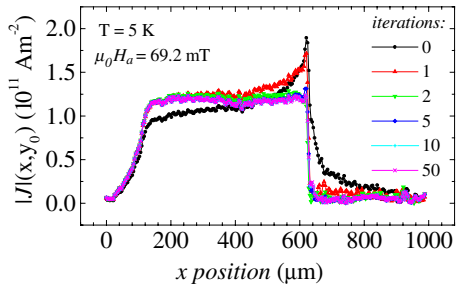

(*a*)

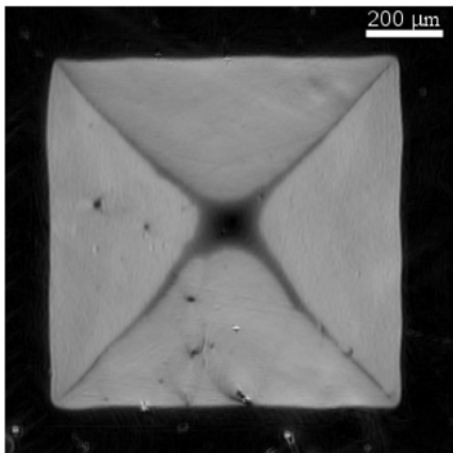

(*b*)

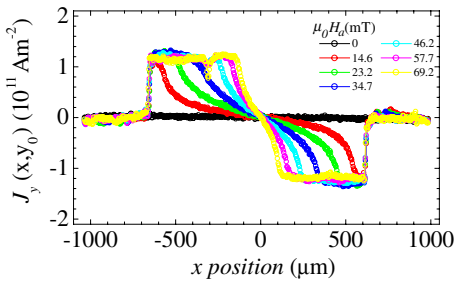

(*c*)

Figure 13. Result of the iterative procedure for the in-plane field effect correction. (*a*) Electrical current density modulus distribution from the same MO image of figure 10(*c*). Outside the sample, the values of current density are strongly reduced and the spurious signal is due to the imperfections of the indicator film. (*b*) Iteration result for the current density modulus. For the sake of readability, only the right part of the profiles is displayed. (*c*) Series of current density modulus profiles traced along the same line of the profiles of figure 11.

The main difference concerns the shape of the current density profile inside the sample, dependent on the space coordinates, hence of the local magnetic induction. The behaviour drastically changes with the correction: from *monotonically increasing towards the edges with positive curvature* to an almost constant, Bean-like, current density value, see figure 13(*b*).

It turns out, in our experiment, that the in-plane field exceeds locally the 40% of B_A (over the sample region), namely this was roughly the previous error on the magnetic induction estimation inside the superconducting film. The error on the current density distribution is even more drastic, because it

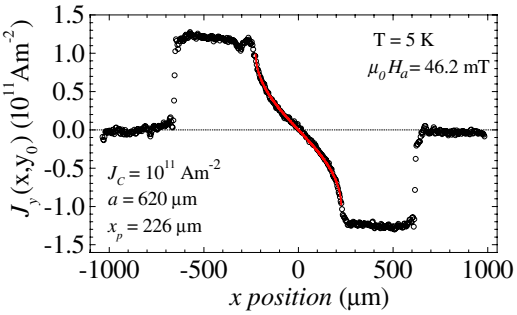

Figure 14. Profile of the electrical current density (y component) at $T = 5$ K and $\mu_0 H_{ext} = 46.2$ mT. In the critical state neither the Bean-like nor the Kim-like trend takes into account the observed small slope of the critical current (decreasing with local magnetic field), but in the Meissner zone a simple equation (7.1) describes very well the experimentally determined values of the current density. The solid curve is calculated with the parameter values show in the graph.

depends on the current density flow pattern, i.e. both on local (structural) and on non-local (geometrical) properties.

To make a first comparison between the corrected current density distribution with simple theoretical models, a set of line profiles was traced along the middle section of the magnetic flux diffusion front. In this way, the Lorenz forces generated by the electrical current flowing in opposite quadrants annul each other and the electrodynamic fields can be approximated by the *strip geometry* [18]. In particular, the Meissner current is simply described by

$$J_M(x) = \frac{2J_C}{\pi} \arctan \frac{x}{a} \frac{\sqrt{(a^2 - x_p^2)}}{\sqrt{(x_p^2 - x^2)}} \qquad (7.1)$$

where J_C is the current density value at the flux front edge, a is the half-width of the square (strip) and x_p is the penetration depth of the vortices inside the superconductor. For a given profile we take the average value of J_C, x_p and a between the two flux fronts. The straight calculus of equation (7.1) and the corresponding experimental profile are shown in figure 14. The agreement is quite satisfying, if we consider that the investigated sample geometry is not so regular. The critical state profile, i.e. the region of higher current density, seems to be almost constant. The little discrepancies with the Bean critical state model [19] come mainly from the sample transverse geometry [20] and they will be discussed in detail in a future work. Now, we note that without the correction the actual critical current density cannot be deduced, since the value at the edge is over 200% of that at the Meissner zone boundary.

8. Conclusion

We demonstrated the importance of the in-plane field effect for the quantitative MO analysis of thin flat superconducting samples. We presented a 2D iterative algorithm which corrects the MO data and reconstructs the current density distribution inside the sample and the full magnetic induction distribution over the superconductor. The new procedure allows evaluating, without artefacts, the local values of the electrical current density that contains essential information about the pinning mechanisms.

Acknowledgments

The YBCO sample was kindly supplied by the joined team 'Edison-Europa Metalli-IMEM/CNR' under a partially funded CNR project (L.95/95). We acknowledge the support of the Istituto Nazionale di Fisica della Materia for partial funding.

References

[1] Koblischka M R and Wijngaarden R J 1995 *Supercond. Sci. Technol.* **8** 199
[2] Polyanskii A A, Feldmann D M and Larbalestier D C 1999 *Handbook of Superconducting Materials* (Bristol: Institute of Physics Publishing) appendix C.3.4
[3] Jooss Ch, Albrecht J, Kuhn H, Leonhardt S and Kronmuller H 2002 *Rep. Prog. Phys.* **65** 651
[4] Goa P E, Hauglin H, Baziljevich M, Il'yashenko E I, Gammel P L and Johansen T H 2001 *Supercond. Sci. Technol.* **14** 729
[5] Dorosinskii L A, Indenbom M V, Nikitenko V I, Ossip'yan Yu A, Polyanskii A A and Vlasko-Vlasov V K 1992 *Physica* C **203** 149
[6] Johansen T H, Baziljevich M, Bratsberg H, Galperin Y, Lindelof P E, Shen Y and Vase P 1996 *Phys. Rev.* B **54** 16264
[7] Helseth L E 2002 *Preprint* cond-mat/0201494
[8] Roth B J, Sepulveda N G and Wkswo J P 1989 *J. Appl. Phys.* **65** 361
[9] Jooss Ch, Warthmann R, Forkl A and Kronmuller H 1998 *Physica* C **299** 215
[10] Helseth L E, Hansen R W, Il'yashenko E I, Baziljevich M and Johansen T H 2001 *Phys. Rev.* B **64** 174406
[11] Gozzelino L, Chiodoni A, Gerbaldo R, Ghigo G, Laviano F, Mezzetti E, Minetti B and Fastampa R 2000 *Int. J. Mod. Phys.* B **14** 2866
[12] Brandt E H 1992 *Phys. Rev.* B **46** 8628
Brandt E H 1995 *Phys. Rev. Lett.* **74** 3025
[13] Xing W, Heinrich B, Zhou H, Fife A A and Cragg A R 1994 *J. Appl. Phys.* **76** 4244
[14] Wijngaarden R J, Spoelder H J W, Surdeanu R and Griessen R 1996 *Phys. Rev.* B **54** 6742
[15] Brandt E H 1995 *Phys. Rev.* B **52** 15442
[16] Jooss Ch, Forkl A, Warthmann R, Habermeier H U, Leibold E and Kronmuller H 1996 *Physica* C **266** 235
[17] Brandt E H 1993 *Phys. Rev.* B **48** 6699
[18] Brandt E H and Indenbom M 1993 *Phys. Rev.* B **48** 12893
[19] Bean C P 1962 *Phys. Rev. Lett.* **8** 250
[20] Mikitik G P and Brandt E H 2000 *Phys. Rev.* B **62** 6800
Mikitik G P and Brandt E H 2000 *Phys. Rev.* B **62** 6812
[21] Schuster Th, Indenbom M V, Koblischka M R, Kuhn H and Kronmüller H 1994 *Phys. Rev.* B **49** 3443